



### **Science Arts & Métiers (SAM)**

is an open access repository that collects the work of Arts et Métiers Institute of Technology researchers and makes it freely available over the web where possible.

This is an author-deposited version published in: <https://sam.ensam.eu>  
Handle ID: <http://hdl.handle.net/10985/6861>

#### **To cite this version :**

Stefania CHERUBINI, Pietro DE PALMA, Alessandro BOTTARO, Jean-Christophe ROBINET -  
Rapid path to transition via nonlinear localized optimal perturbations in a boundary-layer flow -  
Physical Review E - Vol. 82, p.5 - 2010

Any correspondence concerning this service should be sent to the repository

Administrator : [scienceouverte@ensam.eu](mailto:scienceouverte@ensam.eu)



**Rapid path to transition via nonlinear localized optimal perturbations in a boundary-layer flow**S. Cherubini,<sup>1,\*</sup> P. De Palma,<sup>1</sup> J.-Ch. Robinet,<sup>2</sup> and A. Bottaro<sup>3</sup><sup>1</sup>*DIMEG and CEMeC, Politecnico di Bari, via Re David 200, 70125 Bari, Italy*<sup>2</sup>*DynFluid, Arts et Métiers ParisTech, 151, Bd. de l'Hopital, 75013 Paris, France*<sup>3</sup>*DICAT, University of Genova, via Montallegro 1, 16145 Genova, Italy*

(Received 30 July 2010; revised manuscript received 19 October 2010; published 2 December 2010)

Recent studies have suggested that in some cases transition can be triggered by some purely nonlinear mechanisms. Here we aim at verifying such an hypothesis, looking for a localized perturbation able to lead a boundary-layer flow to a chaotic state, following a nonlinear route. Nonlinear optimal localized perturbations have been computed by means of an energy optimization which includes the nonlinear terms of the Navier-Stokes equations. Such perturbations lie on the turbulent side of the laminar-turbulent boundary, whereas, for the same value of the initial energy, their linear counterparts do not. The evolution of these perturbations toward a turbulent flow involves the presence of streamwise-inclined vortices at short times and of hairpin structures prior to breakdown.

DOI: [10.1103/PhysRevE.82.066302](https://doi.org/10.1103/PhysRevE.82.066302)

PACS number(s): 47.20.-k, 47.27.-i

Over 20 years have passed from the first linear transient growth analysis for a Poiseuille or a Couette flow [1]. Since then, with the development of the global-mode theory [2] and of efficient optimization techniques [3] and thanks to the remarkable increase in computing power, a scenario of transient disturbance amplification has been outlined. Typically, one searches for the most effective path to transition by determining the shape of an initial (small) disturbance which yields the maximum energy amplification at a given target time. For the case of boundary-layer flows at low Reynolds number of interest here, the result, obtained in a parallel flow setting, is that linear optimal perturbations consist of pairs of counter-rotating streamwise vortices, capable to elicit streamwise streaks by the lift-up effect [4]. On the basis of such linear results, some authors [5] have argued that the non-normality of the linearized operator is the primary cause of the onset of transition, whereas nonlinearities mostly prevent the viscous decay of the optimally growing disturbances. Nonetheless, later work [6] has demonstrated that the linear mechanism which yields streamwise-homogeneous streaks cannot trigger transition in the absence of nonlinear interactions. Recently, it has been shown [7] that, for a non-parallel Blasius boundary-layer base flow at low Reynolds number, localized optimal perturbations computed by a linear global approach are streamwise modulated. Moreover, they induce transition more effectively than streamwise-independent initial disturbances via a mechanism including the formation of hairpin vortices. Evidence for the preponderance of hairpin-shaped structures in transitional boundary-layer flows abounds (e.g., [8]), proving that nonlinear mechanisms are crucial in the transition scenario. For this reason, several authors [9–17] have tried to follow a different route to discover the basic mechanisms of flow transition by using purely nonlinear analyses. Focus has been in particular onto exact nonlinear solutions of the Navier-Stokes equations, likely to be visited with some regularity by a flow in the course of its chaotic phase-space trajectory.

Among such nonlinear states, one should distinguish those sitting on the edge hypersurface [13], the first states to be approached by the flow during transition. Recently, some studies have been carried out aimed at finding special initial disturbances which cause the disturbed velocity field to approach such coherent structures (the lower-branch solution in a pipe flow in [15] and the edge-state in a plane Couette flow in [16]). In these studies, special perturbations are built by a linear combination of a limited number of “basic modes,” whose coefficients are determined by an optimization procedure. Here, a more general technique to find global optimal perturbations which induce transition efficiently is introduced. For this purpose, avoiding any *a priori* constraint on the shape of the perturbation, we use a global approach extending the linear transient growth analysis of Cherubini *et al.* [7] to the nonlinear framework for the case of a boundary-layer flow. In particular, the three following issues are addressed: (i) prove the existence of a nonlinear amplification mechanism of the disturbances which is more effective with respect to the linear one and capable to lead the flow to turbulence for lower values of the perturbation amplitude; (ii) investigate the structure of the perturbations capable of inducing such an optimal amplification and their nonlinear evolution; (iii) set the basis to establish a link between the nonlinear optimal and the laminar-turbulent boundary in phase space. It is noteworthy that the present analysis refers to a spatially inhomogeneous, open base flow, namely, the Blasius boundary-layer flow,  $\mathbf{U}(x,y)$ . For such a flow, no exact coherent solution nor the structure of the laminar-turbulent boundary has been determined yet.

In order to address the issues above, we seek for the velocity perturbation  $\mathbf{u}$  at  $t=0$ , having a given initial energy  $E_0$ , which can induce at a target time  $T$  the highest perturbation energy  $E(T)=\langle \mathbf{u}(T) \cdot \mathbf{u}(T) \rangle$ , where the symbol  $\langle \rangle$  indicates integration over the considered three-dimensional domain. This *optimal* perturbation is computed by means of a Lagrange multiplier optimization, which consists in finding extrema of the augmented functional

\*s.cherubini@gmail.com

$$\mathcal{L} = \frac{E(T)}{E(0)} - \int_0^T \langle p^\dagger \cdot \nabla \mathbf{u} \rangle dt - \int_0^T \left\langle \mathbf{u}^\dagger \cdot \left\{ \frac{\partial \mathbf{u}}{\partial t} + \mathbf{u} \cdot \nabla \mathbf{u} + \mathbf{U} \cdot \nabla \mathbf{u} + \mathbf{u} \cdot \nabla \mathbf{U} + \nabla p - \frac{\nabla^2 \mathbf{u}}{\text{Re}} \right\} \right\rangle dt - \lambda \left( \frac{E_0}{E(0)} - 1 \right). \quad (1)$$

In Eq. (1), the Navier-Stokes equations in a perturbative formulation have been imposed as constraint;  $(\mathbf{u}^\dagger, p^\dagger)$  are the Lagrange multipliers, e.g., the adjoint variables. The Reynolds number is defined as  $\text{Re} = U_\infty \delta^* / \nu$ , where  $\nu$ ,  $\delta^*$ , and  $U_\infty$  are the kinematic viscosity, the inflow boundary-layer displacement thickness, and the free stream velocity, respectively. The three-dimensional perturbation vanishes at bottom and upper-boundary points, whereas periodicity is imposed in the spanwise homogeneous direction. Since the flow is not periodic in the streamwise direction, a zero perturbation condition is imposed at inflow and outflow; this allows a  $x$ -localized initial disturbance field  $\mathbf{u}(0)$ . In order to avoid the propagation of spurious oscillations inside the computational domain, the zero perturbation condition at the inflow and outflow is enforced by means of two fringe regions, external to the optimization domain, which allow the perturbation to vanish smoothly. The inflow points of the optimization domain are placed at  $x_{in}=200$  with respect to the leading edge of the plate. Integrating by parts and setting to zero the first variation in  $\mathcal{L}$  with respect to  $(\mathbf{u}, p)$  leads to the adjoint equations plus the compatibility condition. The adjoint equations are linked to the direct ones by the presence of direct variables in the advection terms; thus, the whole direct-variable field needs to be stored at each time step, requiring a remarkable storage capacity. The optimization procedure for a chosen target time  $T$  can be summarized as follows:

- (1) An initial guess is taken for the initial condition,  $\mathbf{u}(0)$ , with an associated initial energy  $E_0$ .
- (2) The direct problem is integrated up to  $t=T$ .
- (3) The adjoint variables,  $\mathbf{u}^\dagger(T)$ , are provided by the compatibility condition  $2\mathbf{u}(T)/E(0) - \mathbf{u}^\dagger(T) = 0$ .
- (4) The adjoint problem is integrated backward in time from  $t=T$  to  $t=0$ .
- (5) At  $t=0$ , the initial direct state is updated in the direction of the conjugate gradient, where the gradient of  $\mathcal{L}$  with respect to  $\mathbf{u}(0)$  is  $\partial \mathcal{L} / \partial \mathbf{u}(0) = -2\mathbf{u}(0)(\langle \mathbf{u}(T) \cdot \mathbf{u}(T) \rangle - \lambda E_0) / \langle \mathbf{u}(0) \cdot \mathbf{u}(0) \rangle + \langle \mathbf{u}^\dagger(0) \rangle$ .
- (6) The objective function  $E(T)$  is evaluated: if its variation between two successive iterations is smaller than a chosen threshold  $e$  the loop is stopped, otherwise the procedure is restarted from step (2).

A similar procedure has been used very recently for the case of the parallel flow in a pipe [17]. The direct and adjoint equations are integrated by a second-order-accurate fractional step method using a staggered grid [18]. A second-order-accurate centered space discretization is used. An optimization domain having  $L_x=200$ ,  $L_y=20$ , and  $L_z=10.5$  has been chosen,  $x$ ,  $y$ , and  $z$  being the streamwise, the wall-normal and the spanwise directions, respectively. After a grid-convergence analysis, a mesh made up by  $901 \times 150$

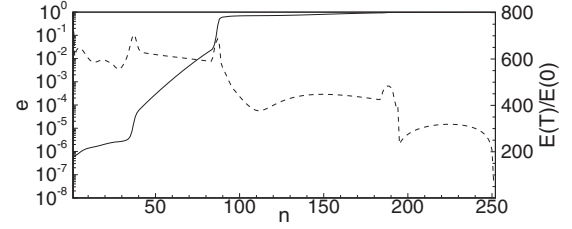


FIG. 1. Energy gain (solid line) and its increment (dashed line) versus the number of iterations for  $E_0=0.01$  and  $T=75$ . The initial guess is the linear global optimal perturbation.

$\times 61$  points—stretched in the wall-normal direction so that the thickness of the first cell close to the wall is equal to 0.1—is selected. The optimizations for initial energy  $E_0=0.01$  and  $T \leq 75$  have been iterated up to a threshold value  $e=10^{-8}$ , which corresponds to a velocity field converged within machine accuracy. It has been verified that, for a larger convergence threshold  $e=10^{-6}$ , the value of  $E(T)$  varies only by 0.5%, and the shape of the optimal perturbation does not show noticeable differences so that the optimizations for higher times and energies (which are more costly) have been iterated up to a threshold value  $e=10^{-6}$ . Nonlinear optimizations have been performed at  $\text{Re}=610$  for two different initial energies,  $E_0=0.1$  and  $E_0=0.01$ . Figure 1 provides the energy gain (solid line) and its increment  $e = [E(T)^n - E(T)^{n-1}] / E(T)^n$  (dashed line) versus the number of iterations,  $n$ , for  $T=75$  and  $E_0=0.01$ . The initial guess is the perturbation obtained by a linear global optimization at the same target time. The procedure converges toward the nonlinear optimal in  $n=250$  iterations going through two “saddle points” (at  $n \approx 35$  and  $n \approx 85$ ; easily distinguishable because  $e$  increases sharply). The length and slope of the plateau and the variation in the velocity field between two successive steps being within machine accuracy at convergence, there is a strong indication that the optimization procedure has indeed identified the global nonlinear optimal initial state. The circles in Fig. 2 show the values of the optimal energy gain computed for  $E_0=0.01$  at five target times, whereas the squares show the results of the corresponding linear optimization. Up to  $T=50$ , the nonlinear energy gain and the shape of the perturbation change but slightly with respect to the linear ones. On the other hand, for larger values of the target time, a strong increase in the energy gain is observed in the

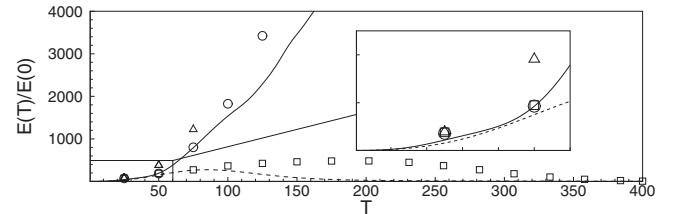


FIG. 2. Optimal energy gain for a target time  $T$ : linear case (squares); nonlinear case for the initial energy  $E_0=0.1$  (triangles) and  $E_0=0.01$  (circles). The solid and dashed lines are the energy gain curves obtained by a DNS initialized with the linear optimal perturbation (dashed line) and with the nonlinear one (solid line), both computed for  $T=75$ , assigning initial energy  $E_0=0.01$ . The inset shows a detail of the curves.

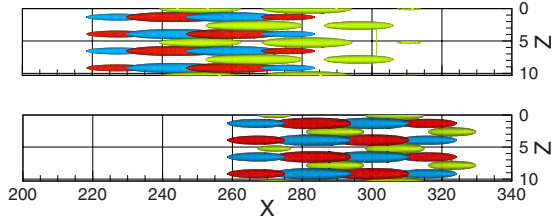


FIG. 3. (Color online) Isosurfaces of the velocity components of the perturbation obtained by the linear optimization for the target time  $T=75$ , for an initial energy  $E_0=0.01$ . Light gray (green) indicates the streamwise component ( $u=-0.00015$  at  $t=0$  and  $u=-0.1$  at  $t=75$ ); gray (blue) and black (red) indicate negative and positive spanwise components, respectively ( $w=\pm 0.004$  at  $t=0$  and  $w=\pm 0.01$  at  $t=75$ ). Axes are not in the same scale.

nonlinear case, reaching a value which is more than six times the linear one for  $T=125$ . For a larger initial energy,  $E_0=0.1$ , a remarkable increase in the energy gain is observed for  $T=50$  and  $T=75$  as shown by the triangles in Fig. 2. This proves the effectiveness of nonlinear effects in inducing a large amplification with respect to configurations characterized by purely linear mechanisms.

Similarly to the energy gain value, also the shape of the optimal perturbations shows large differences with respect to the linear case. Figures 3 and 4 provide the streamwise and spanwise component of the linear and nonlinear optimal perturbations, respectively, at  $t=0$  and  $t=T$ , for the target time  $T=75$ . The linear optimal shows a sinusoidal variation in the spanwise direction; the perturbation is characterized at  $T=0$  by streamwise vortices and at  $t=T$  by streamwise streaks, both modulated in the streamwise direction [7] (although it has been shown in [19] that for larger Reynolds numbers the optimal is a Tollmien-Schlichting wave packet). The nonlinear optimal solution is remarkably different, displaying a short-scale  $x$  modulation, a smaller streamwise extent, and a different spanwise periodicity. It is also important to observe that, for the case under consideration, the nonlinear optimal perturbation does not show noticeable differences when doubling the streamwise length of the optimization domain, unlike the linear case in which the optimal perturbation and energy gain are highly dependent on the streamwise domain length. It has been observed that, for different target times ( $75 \leq T \leq 125$  and  $E_0=0.01$ ) and domain lengths (large

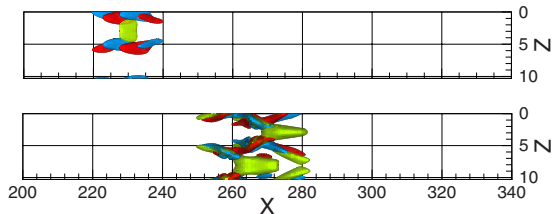


FIG. 4. (Color online) Isosurfaces of the velocity components of the perturbation obtained by the nonlinear optimization for the target time  $T=75$ , for an initial energy  $E_0=0.01$ . Light gray (green) indicates the streamwise component ( $u=-0.01$  at  $t=0$  and  $u=-0.1$  at  $t=75$ ); gray (blue) and black (red) indicate negative and positive spanwise components, respectively ( $w=\pm 0.007$  at  $t=0$  and  $w=\pm 0.05$  at  $t=75$ ). Axes are not in the same scale.

enough for the perturbation not to reach the outflow at the target time), the optimal perturbation is always placed close to the inflow of the domain.

In the first frame ( $t=0$ ) of Fig. 4, one can observe the presence of two series of streamwise-alternated elongated patches of the spanwise component of the perturbation (gray and black surfaces), placed at the two flanks of a low-momentum flow region (light gray surfaces). It is also worth pointing out that, unlike the linear case in which the streamwise component of the initial optimal perturbation is very small, in the nonlinear case the component of the initial velocity perturbation having the highest absolute value is the streamwise one ( $u_{\max}^-=-0.018$  and  $u_{\max}^+=0.011$ ), which is comparable to the spanwise one ( $w_{\max}^-=-0.0163$  and  $w_{\max}^+=0.0163$ ) and rather larger than the wall-normal component ( $v_{\max}^-=-0.0068$  and  $v_{\max}^+=0.0059$ ). Moreover, the regions where the streamwise component of the velocity disturbance is negative are associated with zones of positive wall-normal component, which is not the case for linear optimal perturbations. This means that the amplification of the perturbation is not only due to the lift-up effect, but is strongly affected by nonlinear interactions. In fact, at  $t=T=75$  (see the second frame of Fig. 4), the classical streamwise-elongated streaks are not recovered, but one can observe the presence of a  $\Lambda$  structure which strongly recalls the bulge in the streamwise fluctuation recently described in direct numerical simulations (DNSs) of transition induced by traveling turbulence patches [8]. Such  $\Lambda$  structures are here observed in the wall-normal and streamwise components of the velocity perturbation, whereas the spanwise component shows a sinuous shape along  $x$ . Similar shape and behavior have been found for the optimal perturbation at higher target times for the same initial energy. For this reason, and due to the very large computational cost of the procedure, the optimizations have been performed up to  $T=125$ . Thus, the validity of the present results is limited to initial localized perturbations which can grow in relatively short times, i.e., those most effective in inducing transition. Finally, also for the cases at  $T \geq 50$  and  $E_0=0.1$ , similar structures have been found, although they are more spread out in the spanwise and streamwise direction.

In order to ascertain that the nonlinear optimal disturbances lie on the turbulent side of the laminar-turbulent boundary of the phase space, several DNS initialized by the optimal perturbations have been performed. Figure 2 provides the curves of the energy gain obtained by the DNS initialized with the nonlinear optimal for  $T=75$  and  $E_0=0.01$  (solid line) and with the linear optimal computed for the same target time and with the same initial energy (dashed line). One can observe that the linear optimal perturbation relaminarizes after about 200 time units, whereas the nonlinear one leads the flow to transition. Figure 5 shows the streamwise distribution of the spanwise-averaged skin-friction coefficient  $C_f$  at different times. The laminar and turbulent distributions of  $C_f$  are also reported for comparison. One can observe that, in the core of the propagating wave packet, for  $T > 200$ ,  $C_f$  reaches values which are typical of turbulent flows. It is noteworthy that, at each time instant, a smooth-varying region is observed, recalling the *calm region* typical of the trailing edge of turbulent spots.



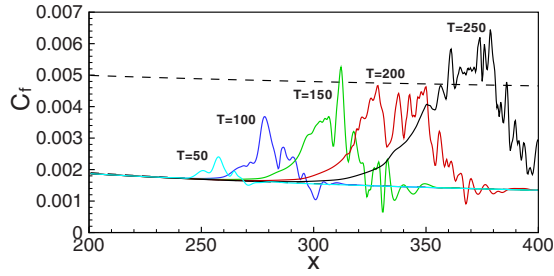


FIG. 5. (Color online) Streamwise distribution of the spanwise-averaged skin-friction coefficient for  $T=50, 100, 150, 200, 250$  (solid lines from left to right) together with the laminar and turbulent theoretical distributions (bottom and top dashed lines, respectively).

One can conclude that, for such rather low value of the initial energy, the nonlinear optimal perturbation computed lies in the basin of attraction of the turbulent flow, whereas the linear one is in the basin the attraction of the laminar fixed point. Therefore, the addition of the nonlinear terms to the optimization procedure has brought the optimal perturbation from one side to the other of the laminar-turbulent boundary in phase space, for the same initial energy. Incidentally, it is worth to notice that the perturbation energy keeps growing until the perturbation is advected by the mean flow outside the domain, due to the spreading of the disturbances upstream and downstream of the main wave packet. Thus, we do not observe in this DNS a state in which the energy oscillates around a fixed value, as in the case of the pipe flow with periodicity in the streamwise direction [13].

Figure 6 shows snapshots of the vortical structures identified by the  $Q$ -criterion [20] (light gray surfaces) and of the

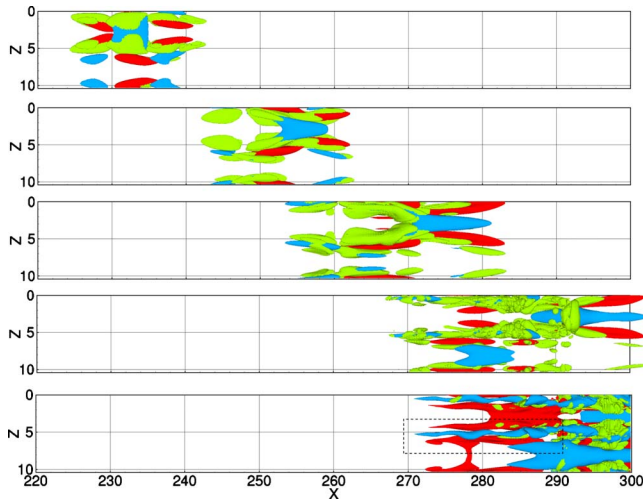


FIG. 6. (Color online) Snapshots of the perturbation at  $t=0, 35, 65, 95$ , and  $125$  obtained by the DNS initialized by the nonlinear optimal for  $T=75$  and  $E_0=0.01$ . The light gray (green) isosurfaces refer to the  $Q$  criterion; the gray (blue) and black (red) isosurfaces refer to the negative and positive values of the streamwise velocity component, respectively. Each variable has been normalized using its maximum value at each time. Isosurfaces show the values  $Q=0.07$  and  $u=\pm 0.5$  at all times except for the snapshot at  $t=125$  showing  $u=\pm 0.25$ .

streamwise component of the perturbation (gray and black surfaces) extracted from the DNS at times  $t=0, 35, 65, 95$ , and  $125$ . The first frame shows the presence of alternated quasistreamwise vortices, which present an inclination in the  $(x, z)$  plane of about  $4^\circ$  with respect to the streamwise direction, whereas in the linear case they are aligned with  $x$ . These vortices are tilted in the streamwise direction by the Orr mechanism, presenting at  $t=35$  (second frame) an inclination of about  $10^\circ$  in the  $(x, y)$  plane (not shown). Due to such an inclination, the downstream part of the vortex, which lies away from the wall, is convected downstream faster than the upstream part because it experiences higher base flow velocity; this causes the stretching and the amplification of such structures, which take the form of  $\Lambda$  vortices. These recall the ones found prior to breakdown in [8] and in the oblique-transition scenario in [21]. At the same time, such vortices induce patches of high and low velocities via the transport of the momentum associated with the base flow and with the finite amplitude streamwise perturbation.

Due to the initial inclination of the vortices, base-flow transport does not induce streamwise streaks but rather it generates  $\Lambda$ -shaped low-momentum regions alternated to high-momentum sinuous ones. At  $t=65$  (third frame) the vortices are further stretched in the streamwise direction, so that the two structures placed on the flanks of the low-momentum region approach one another in their downstream part. A vortex filament oriented in the spanwise direction (the arch) is formed and it connects the two quasistreamwise vortices, inducing the formation of an hairpin, whose head is clearly visible at  $t=95$  (despite the fact that the vortices are breaking up into smaller patches of vorticity, and an elongated low-momentum zone appears under the legs of the hairpin). Thus, it seems that the formation of an arch connecting two isolated streamwise vortices is the primary cause of breakdown, because it induces the rupture of the  $\Lambda$  structures into smaller zones of low momentum. Moreover, the formation of a streamwise streak seems to be a consequence of the creation of the hairpin vortex, corroborating the hypothesis [8] that, in the presence of non-negligible nonlinear effects, streamwise streaks are only a kinematic feature induced by the presence of the hairpin vortices. Such a behavior is recovered for all of the target times considered here, with  $75 \leq T \leq 125$ ; nonetheless, we cannot be sure that for larger target times and/or different initial energies the mechanism could be the same. In order to further validate these results, the spanwise spacing of the low-speed streaks has been measured at  $t=200$  when a turbulent spot is established in the flow. Normalizing the spanwise spacing with respect to the wall shear stress, one obtains  $\lambda^+ \approx 114.5$ , which is close to the streak spacing found in the literature [22]. It is worth remarking that such a spacing is not imposed by the spanwise domain length. Moreover, after the breakdown and upstream of the incipient turbulent spot, sinuous streamwise structures are observed at all times, the dashed rectangle in the bottom frame of Fig. 6 showing an example. Such structures are reminiscent of a class of traveling waves recently obtained for Couette flow [23]. Thus, it is possible that, being on the turbulent side of the laminar-turbulent edge, the nonlinear optimal perturbation evolves into a trajectory which visits exact coherent solutions.

In this paper we have shown that in a boundary-layer flow nonlinear mechanisms exist capable of inducing an energy amplification much larger than the linear one. Optimal perturbations have been computed for different times and energies; most of them are found to lie in the basin of attraction of the turbulent flow for lower levels of the initial energy than their linear optimal counterparts. Such perturbations are localized in the streamwise and spanwise direction and characterized at  $t=0$  by a series of streamwise alternated vortices, slightly inclined with respect to the streamwise direction. The optimal initial perturbations are highly amplified in time by the stretching of the quasistreamwise vortices, induced by the wall-normal shear and by the transport of the base-flow

momentum. The quasistreamwise vortices are then connected by a spanwise vortex filament, originating an hairpin vortex which induces a low-speed streak between its legs. Such a coherent structure is maintained for some time, until a fully turbulent state ensues. Such results confirm those obtained by DNS [8], showing that, even when it is not initialized by the optimal perturbation, the flow reaches transition following a route which approximates the optimal one. This suggests that (i) a preferential route exists, connecting the laminar to the turbulent states and visiting exact coherent structures and that (ii) such a route does not rely on the presence of streamwise-invariant streaks nor vortices.

- 
- [1] B. Farrell, *Phys. Fluids* **31**, 2093 (1988).
  - [2] J. M. Chomaz, *Annu. Rev. Fluid Mech.* **37**, 357 (2005).
  - [3] P. Luchini, *J. Fluid Mech.* **404**, 289 (2000).
  - [4] M. T. Landahl, *J. Fluid Mech.* **98**, 243 (1980).
  - [5] J. S. Baggett, T. A. Driscoll, and L. N. Trefethen, *Phys. Fluids* **7**, 833 (1995).
  - [6] F. Waleffe, *Phys. Fluids* **7**, 3060 (1995).
  - [7] S. Cherubini, J.-C. Robinet, A. Bottaro, and P. De Palma, *J. Fluid Mech.* **656**, 231 (2010).
  - [8] X. Wu and P. Moin, *J. Fluid Mech.* **630**, 5 (2009).
  - [9] M. Nagata, *Phys. Rev. E* **55**, 2023 (1997).
  - [10] F. Waleffe, *Phys. Rev. Lett.* **81**, 4140 (1998).
  - [11] H. Faisst and B. Eckhardt, *Phys. Rev. Lett.* **91**, 224502 (2003).
  - [12] B. Hof, C. van Doorne, J. Westerweel, F. Nieuwstadt, H. Faisst, B. Eckhardt, H. Wedin, R. Kerswell, and F. Waleffe, *Science* **305**, 1594 (2004).
  - [13] B. Eckhardt, T. M. Schneider, B. Hof, and J. Westerweel, *Annu. Rev. Fluid Mech.* **39**, 447 (2007).
  - [14] H. Wedin and R. Kerswell, *J. Fluid Mech.* **508**, 333 (2004).
  - [15] D. Viswanath and P. Cvitanovic, *J. Fluid Mech.* **627**, 215 (2009).
  - [16] Y. Duguet, L. Brandt, and B. R. J. Larsson, *Phys. Rev. E* **82**, 026316 (2010).
  - [17] C. C. T. Pringle and R. Kerswell, *Phys. Rev. Lett.* **105**, 154502 (2010).
  - [18] R. Verzicco and P. Orlandi, *J. Comput. Phys.* **123**, 402 (1996).
  - [19] A. Monokrousos, E. Akervik, L. Brandt, and D. S. Henningson, *J. Fluid Mech.* **650**, 181 (2010).
  - [20] J. C. R. Hunt, A. Wray, and P. Moin, Center for Turbulence Research Report No. CTR-S88, 1988 (unpublished).
  - [21] S. Berlin, M. Wiegel, and D. S. Henningson, *J. Fluid Mech.* **393**, 23 (1999).
  - [22] S. J. Kline, W. C. Reynolds, F. Schraub, and P. Rundstander, *J. Fluid Mech.* **30**, 741 (1967).
  - [23] T. M. Schneider, J. F. Gibson, and J. Burke, *Phys. Rev. Lett.* **104**, 104501 (2010).